BUTTERWORTH HEINEMANN

Numerical simulation of free convective flow using the lattice-Boltzmann scheme

J. G. M. Eggels and J. A. Somers
Koninklijke/Shell-Laboratorium, Amsterdam, The Netherlands

Free convective flow in a square cavity at $Ra = 10^6$ and $Pr = 0.71$ is considered using the lattice–Boltzmann discretization scheme. This scheme is a new type of simulation method for solving the time-dependent Navier–Stokes equations in an incompressible flow regime. It has been extended by a scalar transport equation and by a coupling of the scalar quantity with the momentum equations to enable simulations of nonisothermal flows. A fairly simple flow configuration with fixed temperature vertical walls and adiabatic horizontal walls has been selected as a test case to study the performance of the extended lattice-Boltzmann scheme. Various flow quantities related to different regions of the convective flow, such as vertical and horizontal boundary layers and the core region, agree well with benchmark data and demonstrate the potential of the lattice–Boltzmann scheme for numerical simulations of flows with (multicomponent) scalar transport.

Keywords: numerical simulation; lattice–Boltzmann scheme; free convective flow

Introduction

The lattice–Boltzmann discretization scheme is a new type of direct simulation method for solving the time-dependent Navier–Stokes equations in an incompressible flow regime. The technique originates from the kinetic theory of lattice gases. The continuous flow equations are derived from a discrete version of the Boltzmann equation that describes the macroscopic behavior of a microscopic world of particles moving on a finite lattice (Frisch et al. 1987). Various authors have demonstrated the potential of the lattice–Boltzmann technique, considering numerical accuracy, numerical robustness, flexibility with respect to complex boundaries, computational efficiency, and the high spatial and temporal resolutions that can be achieved on given computer resources (McNamara and Zanetti 1989; Succi et al. 1992; Chen et al. 1992; Somers 1993). When an appropriate subgrid scale (SGS) turbulence model is incorporated, large-eddy simulations of complex turbulent flows at Reynolds numbers of above 100,000 can be performed on three-dimensional (3-D) grids using moderate resolutions of less than a million grid points.

This paper presents the first results of our effort to incorporate convective and diffusive scalar transport into the lattice–Boltzmann discretization scheme. The ultimate objective is to include heat and mass transport capabilities into our lattice–Boltzmann large-eddy simulation tool to study engineering problems encountered in complex turbulent flows. Massaioli et al. (1993) have already reported simulations of thermal flows using the lattice–Boltzmann scheme, focusing on the probability density function of temperature fluctuations in low-Rayleigh number Rayleigh–Bénard convection. The present work, in contrast, considers the steady flow in a square cavity with heated and cooled side walls in which a proper description of the flow in the thin vertical boundary layers is the critical issue. In addition to a complete description of the implementation of the momentum and scalar transport equations in the lattice–Boltzmann framework, the present results are compared in detail with numerical results obtained using different numerical techniques.

The next section of this paper recapitulates the lattice–Boltzmann discretization and briefly describes how a possible subgrid-scale turbulence model fits in. An extension of the scheme with a scalar transport equation is then proposed, and the boundary conditions for the momentum and scalar transport equations are addressed. Finally, a numerical validation of the implementation of the scalar transport equation and the coupling between the scalar quantity and the momentum equations is presented for a free convective flow in a square cavity.

Lattice-Boltzmann equation

The lattice–Boltzmann equation specifies the ensemble average behavior of a lattice gas in which discrete particles of unit mass move with unit speed along the edges of a regular lattice (McNamara and Zanetti 1989). Two- and three-dimensional (2-D and 3-D) projections of the four-dimensional (4-D) face-centered–hyper-cubic (FCHC) lattice are commonly used for simulations of the Navier–Stokes equations (d'Humières et al. 1986). This FCHC lattice spans a 4-D space with 24 velocity directions $\mathbf{c}_i$ at each grid point. Figure 1 depicts the 2-D and 3-D projections of this lattice with 9 and 18 velocity directions $\mathbf{c}_i$, respectively, and weight factors m_i representing the multiplicity of the edges caused by the projection.

The lattice–Boltzmann scheme solves the lattice–Boltzmann equation directly without instantiating a discrete lattice gas, but operationally the procedure is very similar. A dimensionless mass density N_i is associated with each velocity direction $\mathbf{c}_i$ at each position $\mathbf{x}$ and time t. The evolution of the scheme involves two steps: a propagation step that shuffles all variables so that mass density N_i at position $\mathbf{x}$ moves to position $\mathbf{x} + \mathbf{c}_i$, and a collision

Address reprint requests to Dr. J. G. M. Eggels, Koninklijke/Shell-Laboratorium, Amsterdam, Shell Research B. V., P.O. Box 38000, 1030 BN Amsterdam, The Netherlands.

Received 16 January 1995; accepted 1 May 1995

Int. J. Heat and Fluid Flow 16: 357–364, 1995

655 Avenue of the Americas, New York, NY 10010

0142-727X/95/$10.00
SSDI 0142-727X(95)00052-R

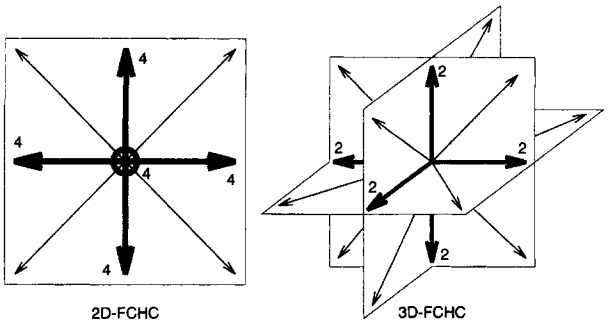

Figure 1 The two- and three-dimensional projections of the face-centered-hyper-cubic lattice correspond to an ordinary square and cubic lattice with 9 and 18 velocity directions $\mathbf{c}_i$, respectively; the numbers along the edges indicate their multiplicities m_i, which, according to the original four-dimensional lattice, satisfy $\Sigma_i m_i = 24$

step that redistributes the mass densities among the velocity directions at each grid point locally. Basically, the scheme solves the following set of coupled partial differential equations:

$$\partial_t N_i + \mathbf{c}_i \cdot \nabla N_i = \Omega_i(\mathbf{N}) \tag{1}$$

The so-called collision operator $\Omega_i(\mathbf{N})$ will depend in a nonlinear way on all components of the mass density vector $\mathbf{N}$ and is constrained by the basic conservation laws of mass and momentum:

$$\sum_i \Omega_i(\mathbf{N}) = 0 \qquad \sum_i \mathbf{c}_i \Omega_i(\mathbf{N}) = \mathbf{f} \tag{2}$$

The vector $\mathbf{f}(\mathbf{x}, t)$ represents an optional external force that accelerates the flow; e.g., caused by gravity or buoyancy. According to the kinetic theory of lattice gases (Frisch et al. 1987), Equation 1 is equivalent to the Navier–Stokes equations, provided that an Ω_i operator is used that guarantees convergence of the lattice–Boltzmann scheme toward the following equilibrium solution for the $N_i(\mathbf{x}, t)$ variables:

$$\begin{aligned} N_i = \frac{m_i \rho}{24}\{1 + 2\mathbf{c}_i \cdot \mathbf{u} \\ + 3\left[\mathbf{c}_i\mathbf{c}_i : \mathbf{uu} - \tfrac{1}{2}\mathrm{tr}(\mathbf{uu}) + \mathbf{c}_i\mathbf{c}_i : \boldsymbol{\tau} - \tfrac{1}{2}\mathrm{tr}(\boldsymbol{\tau})\right] \\ - 6\nu\left[(\mathbf{c}_i \cdot \nabla)(\mathbf{c}_i \cdot \mathbf{u}) - \tfrac{1}{2}\nabla \cdot \mathbf{u}\right] + \mathscr{O}(u^3, u\nabla u)\} \end{aligned} \tag{3}$$

with $\rho = \rho(\mathbf{x}, t) = \Sigma_i N_i(\mathbf{x}, t)$, $\rho\mathbf{u} = \rho(\mathbf{x}, t)\mathbf{u}(\mathbf{x}, t) = \Sigma_i \mathbf{c}_i N_i(\mathbf{x}, t)$ and ν the kinematic viscosity. * The higher-order terms denoted by $\mathscr{O}(u^3, u\nabla u)$ represent unwanted errors and are considered in more detail later. The turbulent stress tensor $\boldsymbol{\tau}$ is new in our lattice–Boltzmann scheme. It arises from unresolvable velocity fluctuations at a scale smaller than the lattice spacing and accounts for the so-called subgrid scale effects in large-eddy simulations (LES) of turbulent flows. In laminar flows or direct simulations of turbulent flows in which the lattice is capable of resolving all scales of the flow, $\boldsymbol{\tau}$ vanishes (see Eggels 1994 for details).

* All flow variables and fluid properties, such as $\mathbf{u}$, ρ, and ν, are scaled in the lattice–Boltzmann concept to dimensionless quantities within certain ranges (e.g., $\|\mathbf{u}\| < 0.2$, $\rho \sim 8$, and $0.25 < \nu < 0.00001$). In the remainder of this paper, all flow variables and fluid properties are assumed to be dimensionless and scaled in this way, unless stated otherwise.

Notation

a	thermal diffusivity
$c_{i\alpha}$	α-component of $\mathbf{c}_i$
$\mathbf{c}_i, \mathbf{c}_j$	velocity direction vector
C	scalar quantity
E_{ik}, E^I_{ki}	filter matrix and its inverse
$\mathbf{f}$	external force vector
$F^{\pm}$	fourth-order terms
g	non-zero component of $\mathbf{g}$
$\mathbf{g}$	gravitation vector
H	cavity height (= width)
$\mathbf{I}$	identity matrix
m_i	weight factor for direction $\mathbf{c}_i$
n	dimensionality of density vectors (9 in 2-D, 18 in 3-D)
$N_i(\mathbf{x}, t)$, $N_j(\mathbf{x}, t)$	mass density in direction $\mathbf{c}_i$, $\mathbf{c}_j$, respectively
$\mathbf{N}$	mass density vector of length n
Nu	Nusselt number
P	pressure
Pr	Prandtl number
$Q_i(\mathbf{x}, t)$, $Q_j(\mathbf{x}, t)$	scalar density in direction $\mathbf{c}_i$, $\mathbf{c}_j$ respectively
$\mathbf{Q}$	scalar density vector of length n
Ra	Rayleigh number
S	stratification parameter
$S^{\pm}_{1,2,3}$	second-order terms
t	time
T	temperature
T_o	reference temperature
$T^{\pm}_{1,2}$	third-order terms
u	velocity component (horizontal)
u_x, u_y	components of $\mathbf{u}$
$\mathbf{u}$	velocity vector
v	velocity component (vertical)
$\mathbf{x}$, $\mathbf{y}$	position vectors

Greek

$\boldsymbol{\alpha}^{\pm}_k$, $\boldsymbol{\beta}^{\pm}_k$	solution vectors containing flow variables
β	thermal expansion coefficient
γ_2, γ_3	coefficients for reduction of the higher-order terms
$\delta_{\alpha\beta}$	Kronecker delta
ΔT	temperature difference
ν	kinematic viscosity
ρ	density
σ_x, σ_y	components of $\boldsymbol{\sigma}$
$\boldsymbol{\sigma}$	subgrid scale flux vector
τ_{xx}, τ_{xy}, τ_{yy}	components of $\boldsymbol{\tau}$
$\boldsymbol{\tau}$	subgrid scale stress tensor
Ψ_i	scalar density collision operator in direction $\mathbf{c}_i$
Ω_i	mass density collision operator in direction $\mathbf{c}_i$

Substitution of Equation 3 into 1 and carrying out the summation over all i, thereby using $\Sigma_i \Omega_i(\mathbf{N}) = 0$ and the symmetry properties of the FCHC lattice:

$$\Sigma_i m_i = 24$$

$$\Sigma_i m_i c_{i\alpha} = 0$$

$$\Sigma_i m_i c_{i\alpha} c_{i\beta} = 12\delta_{\alpha\beta}$$

$$\Sigma_i m_i c_{i\alpha} c_{i\beta} c_{i\gamma} = 0$$

$$\Sigma_i m_i c_{i\alpha} c_{i\beta} c_{i\gamma} c_{i\epsilon} = 4\delta_{\alpha\beta}\delta_{\gamma\epsilon} + 4\delta_{\alpha\gamma}\delta_{\beta\epsilon} + 4\delta_{\alpha\epsilon}\delta_{\beta\gamma} \tag{4}$$

with $c_{i\alpha}$, $c_{i\beta}$, $c_{i\gamma}$, and $c_{i\epsilon}$ denoting the x-, y-, or z-component of $\mathbf{c}_i$ and $\delta_{\alpha\beta}$ the Kronecker delta, yields the following equation for conservation of mass:

$$\partial_t \rho + \nabla \cdot \rho\mathbf{u} = 0 \tag{5}$$

The equations for conservation of momentum are obtained by multiplication of Equation 1 by $\mathbf{c}_i$ and subsequent substitution of Equation 3. After summation over i using the constraint $\Sigma_i \mathbf{c}_i \Omega_i(\mathbf{N}) = \mathbf{f}$ and the symmetry properties given by Equation 4, we find:

$$\partial_t \rho\mathbf{u} + \nabla \cdot \rho\mathbf{u}\mathbf{u} + \nabla \cdot \rho\boldsymbol{\tau}$$

$$= -\nabla P + \nabla \cdot \rho\nu\left[\nabla\mathbf{u} + (\nabla\mathbf{u})^T\right] - \nabla\left(\tfrac{1}{2}\rho\nu\nabla \cdot \mathbf{u}\right) + \mathbf{f} \tag{6}$$

with the following equation of state for the pressure P:

$$P = \tfrac{1}{2}\rho\left\{1 - \tfrac{1}{2}\left[\mathrm{tr}(\mathbf{u}\mathbf{u}) + \mathrm{tr}(\boldsymbol{\tau})\right]\right\} \tag{7}$$

The higher-order terms in Equation 3 have been neglected in this derivation. Inclusion of these terms would have caused additional terms in Equations 5–7, thereby giving rise to macroscopic fluid flow equations that deviate from the Navier–Stokes equations. For accurate simulations of fluid flows according to the Navier–Stokes equations, it is, therefore, necessary to minimize the effects of the higher-order terms on N_i. How this is achieved in our simulations is discussed later.

Having defined the desired solution for $N_i(\mathbf{x}, t)$ by Equation 3, we still need to specify the collision operator $\Omega_i(\mathbf{N})$ in such a way that the scheme, indeed, converges to this equilibrium solution. Therefore, we consider the staggered formulation of the lattice–Boltzmann equation:

$$N_i\left(\mathbf{x} + \tfrac{1}{2}\mathbf{c}_i,\ t + \tfrac{1}{2}\right) = N_i\left(\mathbf{x} - \tfrac{1}{2}\mathbf{c}_i,\ t - \tfrac{1}{2}\right) + \Omega_i(\mathbf{N}) \tag{8}$$

With help of a Taylor-series expansion of $N_i(\mathbf{x} + \frac{1}{2}\mathbf{c}_i,\ t + \frac{1}{2})$ and $N_i(\mathbf{x} - \frac{1}{2}\mathbf{c}_i,\ t - \frac{1}{2})$:

$$N_i\left(\mathbf{x} \pm \tfrac{1}{2}\mathbf{c}_i,\ t \pm \tfrac{1}{2}\right) = N_i(\mathbf{x},\ t) \pm \tfrac{1}{2}\mathbf{c}_i \cdot \nabla N_i(\mathbf{x},\ t)$$

$$\pm \tfrac{1}{2}\partial_t N_i(\mathbf{x},\ t) + \text{h.o.t.} \tag{9}$$

and substitution of $N_i(\mathbf{x}, t)$ from Equation 3, we obtain:

$$\Omega_i(\mathbf{N}) = N_i\left(\mathbf{x} + \tfrac{1}{2}\mathbf{c}_i,\ t + \tfrac{1}{2}\right) - N_i\left(\mathbf{x} - \tfrac{1}{2}\mathbf{c}_i,\ t - \tfrac{1}{2}\right)$$

$$= \mathbf{c}_i \cdot \nabla N_i(\mathbf{x},\ t) + \partial_t N_i(\mathbf{x},\ t) + \text{h.o.t.}$$

$$= \frac{m_i\rho}{12}\left[(\mathbf{c}_i \cdot \nabla)(\mathbf{c}_i \cdot \mathbf{u}) - \tfrac{1}{2}\nabla \cdot \mathbf{u}\right] + \frac{m_i}{12}\mathbf{c}_i \cdot \mathbf{f} + \text{h.o.t.} \tag{10}$$

thereby using $\partial_t \rho = -\nabla \cdot \rho\mathbf{u}$ and $\partial_t \rho\mathbf{u} = -\frac{1}{2}\nabla\rho + \mathbf{f} + \mathscr{O}(\nabla u^2, \nabla^2 u)$ (Somers 1993). The h.o.t. in Equation 10 contain, among contributions related to the lattice spacing and the time-step, terms of the form $\mathbf{u} \cdot \nabla\rho$, which are small in the incompressible limit. It can easily be verified that the $\Omega_i(\mathbf{N})$ operator of Equation 10 indeed, satisfies the basic conservation laws of Equation 2.

The collision operator shows a great similarity with the viscous term in the equilibrium solution of Equation 3 which makes its implementation in the lattice–Boltzmann scheme fairly straightforward. From Equations 9 and 10 with neglect of the h.o.t., we get:

$$N_i\left(\mathbf{x} \pm \tfrac{1}{2}\mathbf{c}_i,\ t \pm \tfrac{1}{2}\right) = N_i(\mathbf{x},\ t) \pm \tfrac{1}{2}\Omega_i(\mathbf{N}) \tag{11}$$

which can be rewritten in terms of a $n \times n$ filter matrix E_{ik} and a solution vector $\alpha_k^{\pm}(\mathbf{x}, t)$ as:

$$N_i\left(\mathbf{x} \pm \tfrac{1}{2}\mathbf{c}_i,\ t \pm \tfrac{1}{2}\right) = \frac{m_i}{24}\sum_{k=1}^{n} E_{ik}\alpha_k^{\pm}(\mathbf{x},\ t) \qquad i = 1, \ldots, n \tag{12}$$

In two dimensions with $n = 9$, E_{ik} and $\alpha_k^{\pm}(\mathbf{x}, t)$ are given by:

$$E_{ik} = \begin{bmatrix} 1, & 2c_{ix}, & 2c_{iy}, & 3\left(c_{ix}^2 - \frac{1}{2}\right), & 6c_{ix}c_{iy}, & 3\left(c_{iy}^2 - \frac{1}{2}\right), \\ & c_{ix}\left(3c_{iy}^2 - 1\right), & c_{iy}\left(3c_{ix}^2 - 1\right), & 3\left(c_{ix}^2 - c_{iy}^2\right)^2 - 2 & & \end{bmatrix} \tag{13}$$

and

$$\alpha_k^{\pm}(\mathbf{x},\ t) = \begin{bmatrix} \rho,\ \rho u_x \pm \frac{1}{2}f_x,\ \rho u_y \pm \frac{1}{2}f_y, \\ \rho(u_x u_x + \tau_{xx}) + \rho\left(\dfrac{\pm 1 - 6\nu}{6}\right)(2\partial_x u_x), \\ \rho(u_x u_y + \tau_{xy}) + \rho\left(\dfrac{\pm 1 - 6\nu}{6}\right)(\partial_x u_y + \partial_y u_x), \\ \rho(u_y u_y + \tau_{yy}) + \rho\left(\dfrac{\pm 1 - 6\nu}{6}\right)(2\partial_y u_y), \\ T_1^{\pm}, T_2^{\pm}, F^{\pm} \end{bmatrix} \tag{14}$$

We return to the higher-order terms $T_1^{\pm}$ through $F^{\pm}$ later. The matrix E_{ik} is formulated in such a way that its inverse E_{ki}^I can be determined directly as:

$$E_{ki}^I = \begin{pmatrix} 1, & c_{ix}, & c_{iy}, & \frac{3}{2}c_{ix}^2 + \frac{1}{2}c_{iy}^2 - 1, & c_{ix}c_{iy}, & \frac{3}{2}c_{iy}^2 + \frac{1}{2}c_{ix}^2 - 1, \\ & c_{ix}\left(3c_{iy}^2 - 1\right), & c_{iy}\left(3c_{ix}^2 - 1\right), & \frac{3}{2}\left(c_{ix}^2 - c_{iy}^2\right)^2 - 1 & & \end{pmatrix}^T \tag{15}$$

with

$$E_{ki}^I \frac{m_i}{24} E_{ik} = \frac{m_i}{24} E_{ik} E_{ki}^I = \mathbf{I} \tag{16}$$

The procedure for marching in time is now as follows:

First, determine the n elements of the solution vector $\alpha_k^-(\mathbf{x}, t)$ from the known distribution $N_i(\mathbf{x} - \frac{1}{2}\mathbf{c}_i,\ t - \frac{1}{2})$ as:

$$\alpha_k^-(\mathbf{x},\ t) = \sum_{i=1}^{n} E_{ki}^I N_i\left(\mathbf{x} - \tfrac{1}{2}\mathbf{c}_i,\ t - \tfrac{1}{2}\right) \qquad k = 1, \ldots, n \tag{17}$$

Second, compute the elements of $\alpha_k^+(\mathbf{x}, t)$ from $\alpha_k^-(\mathbf{x}, t)$ using Equation 14 and taking into account the following considerations:

(1) The components of the external force vector $\mathbf{f}$ are known, so the velocity components u_x and u_y in $\alpha_k^-(\mathbf{x}, t)$ can be computed. The total stresses can also be computed, but an additional SGS turbulence model is needed for τ_{xx} and others to separate the shear rates $\partial_x u_x$ and so on from the total stresses. The details of possible SGS stress models are beyond the scope of this paper, but can be found in Somers (1993) and Eggels (1994). In the present study, only laminar flows are considered for which $\boldsymbol{\tau}$ (and σ) are zero by definition.

(2) The terms $T_1^{\pm}$, $T_2^{\pm}$, and $F^{\pm}$ in Equation 14 represent two third-order and a fourth-order contribution in Equation 3 and,

in addition, contain the neglected higher-order terms in Equation 9. Especially in low-viscosity regimes, these modes limit the numerical accuracy of the lattice–Boltzmann scheme. However, a more accurate study of the higher-order terms in Equation 9 reveals that T_1 and T_2 merely change sign in the collision step, and hence can be accounted for in the $\Omega_i(\mathbf{N})$ operator. This is achieved by imposing $T_1^+ = -\gamma_3 T_1^-$ and $T_2^+ = -\gamma_3 T_2^-$ with γ_3 an adjustable coefficient of order unity. The advantage of this approach is that the third-order terms $T_{1,2}$ in $\alpha_k(\mathbf{x}, t)$ associated with $N_i(\mathbf{x}, t)$ become of the form $\frac{1}{2}(1-\gamma_3)T_{1,2}^-$. * With γ_3 around 0.8, the leading higher-order terms in $N_i(\mathbf{x}, t)$ are of the order of 0.1 $T_{1,2}^-$ with this approach. A similar approach is not applied for the fourth-order term F because of its smaller magnitude. In general, $F^+ = 0$ is imposed in our simulations.

Third, having determined the elements of $\alpha_k^+(\mathbf{x}, t)$ as

$$\alpha_k^+(\mathbf{x}, t) = \begin{bmatrix} \rho,\ \rho u_x + \frac{1}{2}f_x,\ \rho u_y + \frac{1}{2}f_y, \\ \rho(u_x u_x + \tau_{xx}) + \rho\left(\frac{+1-6\nu}{6}\right)(2\partial_x u_x), \\ \rho(u_x u_y + \tau_{xy}) + \rho\left(\frac{+1-6\nu}{6}\right)(\partial_x u_y + \partial_y u_x), \\ \rho(u_y u_y + \tau_{yy}) + \rho\left(\frac{+1-6\nu}{6}\right)(2\partial_y u_y), \\ -\gamma_3 T_1^-,\ -\gamma_3 T_2^-,\ 0 \end{bmatrix} \tag{18}$$

the filter matrix E_{ik} is used to compute the lattice–Boltzmann variables $N_i(\mathbf{x} + \frac{1}{2}\mathbf{c}_i, t + \frac{1}{2})$ from Equation 12.

Fourth, after this collision step, all lattice–Boltzmann variables $N_i(\mathbf{x} + \frac{1}{2}\mathbf{c}_i, t + \frac{1}{2})$ are shuffled during the propagation step such that the mass density $N_i(\mathbf{x} + \frac{1}{2}\mathbf{c}_i, t + \frac{1}{2})$ associated with the grid point at position $\mathbf{x}$ moves to the grid point at position $\mathbf{x} + \mathbf{c}_i$ to become $N_i(\mathbf{x} - \frac{1}{2}\mathbf{c}_i, t - \frac{1}{2})$ for the next time-step.

Scalar transport in the lattice–Boltzmann framework

To include heat and mass transfer in the lattice–Boltzmann simulations, a scalar transport equation of the form

$$\partial_t \rho C + \nabla \cdot \rho \mathbf{u} C + \nabla \cdot \rho \boldsymbol{\sigma} = \nabla \cdot \rho a \nabla C \tag{19}$$

with $C(\mathbf{x}, t)$ the scalar quantity and a the diffusion coefficient, needs to be solved. The flux vector $\boldsymbol{\sigma}$ accounts for SGS effects in large-eddy simulations and is comparable to the SGS stress tensor $\boldsymbol{\tau}$ in the momentum equations. In analogy to the mass density distribution $N_i(\mathbf{x}, t)$, the scalar density $Q_i(\mathbf{x}, t)$ along velocity direction $\mathbf{c}_i$ is introduced. In a straightforward way $C(\mathbf{x},t)$ is related to $Q_i(\mathbf{x}, t)$ as:

$$\rho(\mathbf{x}, t) C(\mathbf{x}, t) = \sum_i Q_i(\mathbf{x}, t) \tag{20}$$

The evolution of $Q_i(\mathbf{x}, t)$ is again governed by a set of coupled partial differential equations:

$$\partial_t Q_i + \mathbf{c}_i \cdot \nabla Q_i = \Psi_i(\mathbf{Q}) \tag{21}$$

with $\Psi_i(\mathbf{Q})$ the scalar density collision operator, similar to $\Omega_i(\mathbf{N})$ in Equation 1. To derive Equation 19 from 20 and 21, the equilibrium solution for $Q_i(\mathbf{x}, t)$ should be related to ρ, $\mathbf{u}$ and C at position $\mathbf{x}$ and time t as follows:

$$Q_i = \frac{m_i \rho}{24}\left[C + 2\mathbf{c}_i \cdot \mathbf{u}C + 2\mathbf{c}_i \cdot \boldsymbol{\sigma} - 2\mathbf{c}_i \cdot a\nabla C + \mathscr{O}(\nabla^2 C,\ u\nabla C)\right] \tag{22}$$

Equation 19 is now obtained by substituting Equation 22 into Equation 21, neglecting the h.o.t. and carrying out the summation over all i, thereby using the conservative property of the scalar density collision operator $[\Sigma_i \Psi_i(\mathbf{Q}) = 0]$ and the symmetry of the lattice as given by Equation 4.

The analysis presented earlier for the derivation of the collision operator $\Omega_i(\mathbf{N})$ can also be carried out for the scalar collision operator $\Psi_i(\mathbf{Q})$. From the Taylor-series expansion, we then obtain:

$$Q_i\left(\mathbf{x} \pm \tfrac{1}{2}\mathbf{c}_i,\ t \pm \tfrac{1}{2}\right) = Q_i(\mathbf{x}, t) \pm \frac{m_i \rho}{48}\mathbf{c}_i \cdot \nabla C + \mathscr{O}(\nabla^2 C,\ u\nabla C) \tag{23}$$

and consequently:

$$\Psi_i(\mathbf{Q}) = \frac{m_i \rho}{24}\mathbf{c}_i \cdot \nabla C + \text{h.o.t.} \tag{24}$$

To illustrate the minimization of the higher-order modes in the scalar transport scheme, the final result for $Q_i(\mathbf{x} \pm \frac{1}{2}\mathbf{c}_i, t \pm \frac{1}{2})$ in terms of the solution vectors $\beta_k^{\pm}(\mathbf{x}, t)$ with physical modes C, $\partial_x C$ and $\partial_y C$ and the higher-order modes S_1 through F is given here:

$$\beta_k^-(\mathbf{x}, t) = \sum_{i=1}^{n} E_{ki}^I Q_i\left(\mathbf{x} - \tfrac{1}{2}\mathbf{c}_i,\ t - \tfrac{1}{2}\right) \qquad k = 1, \ldots, n \tag{25}$$

and

$$Q_i\left(\mathbf{x} + \tfrac{1}{2}\mathbf{c}_i,\ t + \tfrac{1}{2}\right) = \frac{m_i}{24}\sum_{k=1}^{n} E_{ik}\beta_k^+(\mathbf{x}, t) \qquad i = 1, \ldots, n \tag{26}$$

with E_{ik} as in Equation 13, E_{ki}^1 as in Equation 15 and $\beta_k^{\pm}(\mathbf{x}, t)$ as:

$$\beta_k^-(\mathbf{x}, t) = \begin{pmatrix} \rho C, \\ \rho(u_x C + \sigma_x) + \rho\left(\frac{-1-4a}{4}\right)\partial_x C, \\ \rho(u_y C + \sigma_y) + \rho\left(\frac{-1-4a}{4}\right)\partial_y C, \\ S_1^-,\ S_2^-,\ S_3^-, \\ T_1^-,\ T_2^-,\ F^- \end{pmatrix}$$

$$\beta_k^+(\mathbf{x}, t) = \begin{pmatrix} \rho C, \\ \rho(u_x C + \sigma_x) + \rho\left(\frac{+1-4a}{4}\right)\partial_x C, \\ \rho(u_y C + \sigma_y) + \rho\left(\frac{+1-4a}{4}\right)\partial_y C, \\ -\gamma_2 S_1^-,\ -\gamma_2 S_2^-,\ -\gamma_2 S_3^-, \\ 0,\ 0,\ 0 \end{pmatrix} \tag{27}$$

The density ρ and the velocity components u_x and u_y are known from $\alpha_k^-(\mathbf{x}, t)$ when solving the scalar C and the total fluxes. Again, a turbulence model for the SGS flux components σ_x and σ_y is required to separate the scalar gradients from the

* Recall that $N_i(\mathbf{x}, t) = \frac{1}{2}N_i(\mathbf{x} + \frac{1}{2}\mathbf{c}_i, t + \frac{1}{2}) + \frac{1}{2}N_i(\mathbf{x} - \frac{1}{2}\mathbf{c}_i, t - \frac{1}{2})$ by definition of Equation 9 and that the solution vector $\alpha_k(\mathbf{x}, t)$ thus equals $\frac{1}{2}\alpha_k^+(\mathbf{x}, t) + \frac{1}{2}\alpha_k^-(\mathbf{x}, t)$ because of Equation 12. So, the third-order terms in $\alpha_k(\mathbf{x}, t)$ are equal to: $T_{1,2} = \frac{1}{2}T_{1,2}^+ + \frac{1}{2}T_{1,2}^- = -\frac{1}{2}\gamma_3 T_{1,2}^- + \frac{1}{2}T_{1,2}^- = \frac{1}{2}(1-\gamma_3)T_{1,2}^-$.

total fluxes. The time integration procedure is the same as discussed before for the mass densities: first compute $\beta_k^-(\mathbf{x}, t)$ from $Q_i(\mathbf{x} - \frac{1}{2}\mathbf{c}_i, t - \frac{1}{2})$ using Equation 25, next determine $\beta_k^+(\mathbf{x}, t)$ from $\beta_k^-(\mathbf{x}, t)$ with the aid of Equation 27, then obtain the new scalar densities $Q_i(\mathbf{x} + \frac{1}{2}\mathbf{c}_i, t + \frac{1}{2})$ from Equation 26, and finally shuffle Q_i at every grid point to end up with $Q_i(\mathbf{x} - \frac{1}{2}\mathbf{c}_i, t - \frac{1}{2})$. Similar as for N_i, the magnitude of the second-order modes is suppressed here by taking $0.80 < \gamma_2 < 0.95$. The third- and fourth-order modes $T_{1,2}^+$ and F^+ are taken equal to zero.

Boundary conditions

In all simulations described below, no-slip velocity conditions are imposed on the rigid walls of the cavity. Fixed temperatures (Dirichlet conditions) are prescribed on the vertical walls, whereas the horizontal walls are perfectly insulated (Neumann conditions). These boundary conditions are effectuated in the simulations by proper choices of the mass and scalar densities entering the computational domain through the boundaries during the propagation step.

Suppose that boundary conditions must be imposed at position $\mathbf{x} + \frac{1}{2}\mathbf{c}_i$ (boundaries must coincide with the edges of the lattice), then Equations 3 and 22 can be used to compute $N_i(\mathbf{x} + \frac{1}{2}\mathbf{c}_i, t + \frac{1}{2})$ and $Q_i(\mathbf{x} + \frac{1}{2}\mathbf{c}_i, t + \frac{1}{2})$ at the boundary using ρ, $\mathbf{u}$ and so on at $(\mathbf{x} + \frac{1}{2}\mathbf{c}_i, t + \frac{1}{2})$. Next, we define the mass and scalar densities $N_j(\mathbf{y} + \frac{1}{2}\mathbf{c}_j, t + \frac{1}{2})$ and $Q_j(\mathbf{y} + \frac{1}{2}\mathbf{c}_j, t + \frac{1}{2})$ in direction $\mathbf{c}_j$ on the boundary at position $\mathbf{y} + \frac{1}{2}\mathbf{c}_j$. $N_j(\mathbf{y} + \frac{1}{2}\mathbf{c}_j, t + \frac{1}{2})$ and $Q_j(\mathbf{y} + \frac{1}{2}\mathbf{c}_j, t + \frac{1}{2})$ are appointed as the densities entering the domain at *that* position where $N_i(\mathbf{x} + \frac{1}{2}\mathbf{c}_i, t + \frac{1}{2})$ and $Q_i(\mathbf{x} + \frac{1}{2}\mathbf{c}_i, t + \frac{1}{2})$ leave the domain during propagation. This can only be achieved by enforcing $\mathbf{y} = \mathbf{x} + \mathbf{c}_i$ and $\mathbf{c}_j = -\mathbf{c}_i$, such that $\mathbf{y} + \frac{1}{2}\mathbf{c}_j \equiv \mathbf{x} + \frac{1}{2}\mathbf{c}_i$. The implementation of the boundary conditions has, thus, been shifted toward finding expressions for $N_j(\mathbf{x} + \frac{1}{2}\mathbf{c}_i, t + \frac{1}{2})$ and $Q_j(\mathbf{x} + \frac{1}{2}\mathbf{c}_i, t + \frac{1}{2})$ in terms of $N_i(\mathbf{x} + \frac{1}{2}\mathbf{c}_i, t + \frac{1}{2})$ and $Q_i(\mathbf{x} + \frac{1}{2}\mathbf{c}_i, t + \frac{1}{2})$ together with the conditions at the boundary. The difference between $N_i(\mathbf{x} + \frac{1}{2}\mathbf{c}_i, t + \frac{1}{2})$ and $N_j(\mathbf{x} + \frac{1}{2}\mathbf{c}_i, t + \frac{1}{2})$ can be obtained from Equation 3:

$$N_i\left(\mathbf{x} + \tfrac{1}{2}\mathbf{c}_i, t + \tfrac{1}{2}\right) - N_j\left(\mathbf{x} + \tfrac{1}{2}\mathbf{c}_i, t + \tfrac{1}{2}\right) = \frac{m_i\rho}{6}\{\mathbf{c}_i \cdot \mathbf{u}\} \quad (28)$$

with ρ and $\mathbf{u}$ given at $(\mathbf{x} + \frac{1}{2}\mathbf{c}_i, t + \frac{1}{2})$. For no-slip velocity conditions ($\mathbf{u} = 0$), Equation 28 reduces to:

$$N_j\left(\mathbf{x} + \tfrac{1}{2}\mathbf{c}_i, t + \tfrac{1}{2}\right) = N_i\left(\mathbf{x} + \tfrac{1}{2}\mathbf{c}_i, t + \tfrac{1}{2}\right) \quad (29)$$

which effectuates a "bounce-back" condition for the ensemble average behavior of the particles. For the scalar densities, we find from Equation 22, assuming $\boldsymbol{\sigma} = \mathbf{o}$:

$$Q_i\left(\mathbf{x} + \tfrac{1}{2}\mathbf{c}_i, t + \tfrac{1}{2}\right) - Q_j\left(\mathbf{x} + \tfrac{1}{2}\mathbf{c}_i, t + \tfrac{1}{2}\right) = \frac{m_i\rho}{6}\{\mathbf{c}_i \cdot \mathbf{u}C - \mathbf{c}_i \cdot a\nabla C\} \quad (30)$$

For a perfectly insulated rigid wall with $\mathbf{u}C = a\nabla C = \mathbf{o}$, this reduces to:

$$Q_j\left(\mathbf{x} + \tfrac{1}{2}\mathbf{c}_i, t + \tfrac{1}{2}\right) = Q_i\left(\mathbf{x} + \tfrac{1}{2}\mathbf{c}_i, t + \tfrac{1}{2}\right) \quad (31)$$

To implement a Dirichlet condition for C at a rigid wall, we add the expressions for Q_j and Q_i as given by Equation 22 to obtain:

$$Q_i\left(\mathbf{x} + \tfrac{1}{2}\mathbf{c}_i, t + \tfrac{1}{2}\right) + Q_j\left(\mathbf{x} + \tfrac{1}{2}\mathbf{c}_i, t + \tfrac{1}{2}\right) = \frac{m_i\rho}{12}\{C\} \quad (32)$$

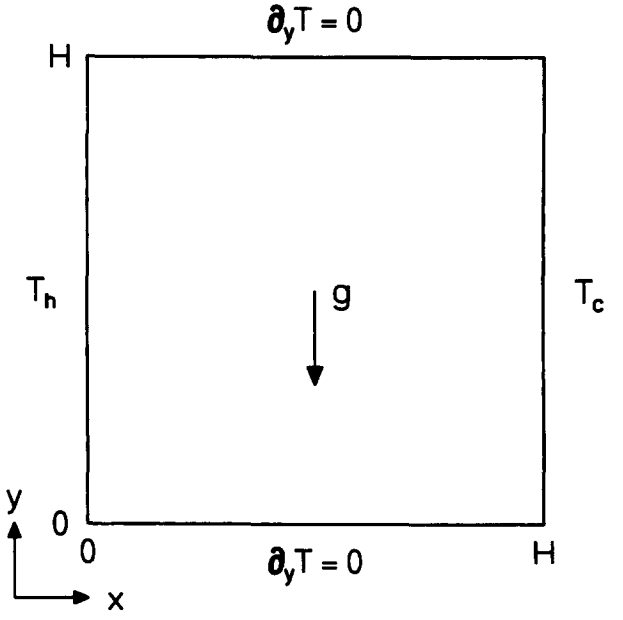

Figure 2 Flow configuration for a free convective flow inside a square cavity with height and width equal to H

with ρ and C again given at $(\mathbf{x} + \frac{1}{2}\mathbf{c}_i, t + \frac{1}{2})$. The incoming scalar densities Q_j are thus, computed as:

$$Q_j\left(\mathbf{x} + \tfrac{1}{2}\mathbf{c}_i, t + \tfrac{1}{2}\right) = \frac{m_i\rho}{12}C - Q_i\left(\mathbf{x} + \tfrac{1}{2}\mathbf{c}_i, t + \tfrac{1}{2}\right) \quad (33)$$

Free convective cavity flow

To evaluate the performance of the lattice–Boltzmann scheme extended with a scalar transport equation and a coupling of the scalar quantity with the momentum equations via the external force vector $\mathbf{f}(\mathbf{x}, t)$, the free convective flow inside a square cavity is considered as a test case. The flow configuration is fairly simple and consists of a 2-D square cavity with a hot vertical wall on one side and a cold vertical wall on the opposite side (see Figure 2). The horizontal bottom and top walls are considered to be perfectly insulated. Detailed numerical benchmark data on this flow configuration are reported by Henkes (1990) and Janssen (1994).

A free convective flow can be characterized by two dimensionless parameters: the Rayleigh number Ra and the Prandtl number Pr

$$\mathrm{Ra} = \frac{g\beta\Delta T H^3}{\nu a} \qquad \mathrm{Pr} = \frac{\nu}{a} \quad (34)$$

with g the acceleration due to gravity, β the coefficient of thermal expansion, ΔT the temperature difference between the two vertical walls and H the height (= width) of the cavity. For the present test case, we restricted ourselves to the laminar regime using $\mathrm{Ra} = 10^6$ and $\mathrm{Pr} = 0.71$ (air). Hence, the SGS stress tensor τ in Equation 3 and the SGS flux vector $\boldsymbol{\sigma}$ in Equation 22 are equal to zero.

The coupling between the scalar quantity (temperature) and the momentum equations is established by means of the Boussinesq approximation. Within this approximation, it is assumed that all fluid properties (density, viscosity, thermal diffusivity) can be considered constant. Small density variations that drive the convective flow as a result of small temperature variations are

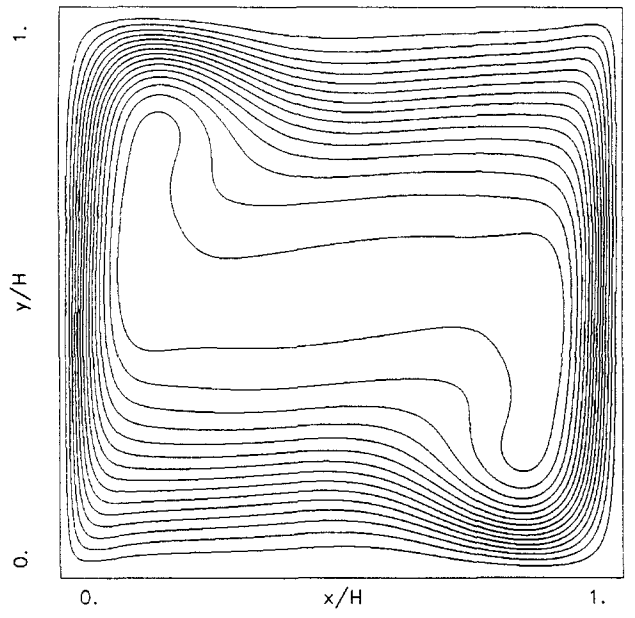

Figure 3 Streamlines of the convective flow in the square cavity at Ra = 10^6 and Pr = 0.71

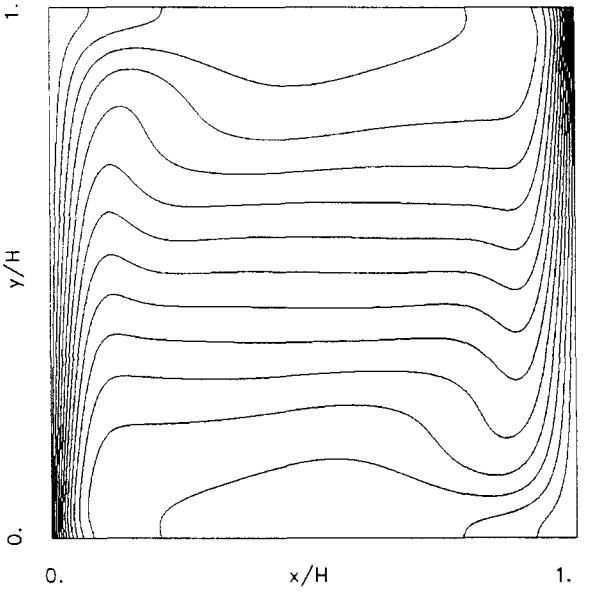

Figure 4 Isotherms of the convective flow in the square cavity at Ra = 10^6 and Pr = 0.71

accounted for in the momentum equations via the force vector **f**, which is directly proportional to the temperature variations:

$$\mathbf{f} = -\rho_{T_o}\mathbf{g}\beta(T - T_o) \tag{35}$$

with T_o a reference temperature. The reason for using the Boussinesq approximation rather than the straightforward relation $\mathbf{f} = \rho_T\mathbf{g}$ is that the temperature does not appear explicitly in the equation of state related to the lattice–Boltzmann scheme. The influence of temperature on density is, therefore, effectuated using Equation 35.

Figures 3 and 4 show the streamlines and isotherms of the convective flow in the cavity, respectively. Vertical flow occurs in the thin boundary layers along the vertical walls. The core region is largely stratified and the velocity magnitudes are small in this region. Temperature and velocity gradients are large in the vertical and, to a lesser degree, horizontal boundary layers and, therefore, sufficient spatial resolution is required near the walls to capture these large spatial variations accurately. A disadvantage of the present discretization scheme is that it only allows for a *uniform* grid throughout the complete computational domain because of the required symmetry of the lattice (see Equation 4). In view of this, the present flow configuration with its thin boundary layers along the vertical walls should be regarded as a severe test case for the lattice–Boltzmann scheme.

To enable a quantitative comparison of the present results with the benchmark data reported by Henkes (1990) and Janssen (1994), four different quantities are listed in Table 1 for various grids: the average heat transfer through the vertical wall in terms of the Nusselt number Nu; the maximum of the vertical velocity v along a horizontal line through the cavity center; the maximum of the horizontal velocity u along a vertical line through the cavity center; and the dimensionless vertical temperature gradient S in the center of the cavity. Following Janssen, Nu and S are defined as:

$$\mathrm{Nu} = -\frac{1}{\Delta T}\int_0^H (\partial_x T)_{x=0}\,\mathrm{d}y \qquad S = \frac{H}{\Delta T}(\partial_y T)_{x=y=\frac{1}{2}H} \tag{36}$$

Table 1 Flow quantities for various grids compared to benchmark data reported by Janssen (1994) using a finite difference/volume technique and Le Quéré (1991) using a pseudospectral method with Chebyshev polynomials. In all simulations, $\gamma_2 = \gamma_3 = 0.80$ (see Equations 18 and 27)

Grid	$\mathrm{NuRa}^{-1/4}$	$\frac{v_{max}}{(g\beta\Delta TH)^{1/2}}$	$\frac{u_{max}}{(g\beta\Delta T\nu)^{1/3}}$	S
30 × 30	0.2812	0.2448	0.7768	0.8662
60 × 60	0.2732	0.2581	0.8071	0.9087
120 × 120	0.2766	0.2615	0.8133	0.9159
240 × 240	0.2783	0.2621	0.8144	0.9176
480 × 480	0.2786	0.2623	0.8145	0.9179
Janssen (1994)				
60 × 60	0.2789	0.2633	0.8145	0.9190
120 × 120	0.2790	0.2621	0.8144	0.9144
240 × 240	0.2791	0.2618	0.8146	0.9132
Le Quéré (1991)				
72 × 72	0.2791	0.2618	0.8146	—

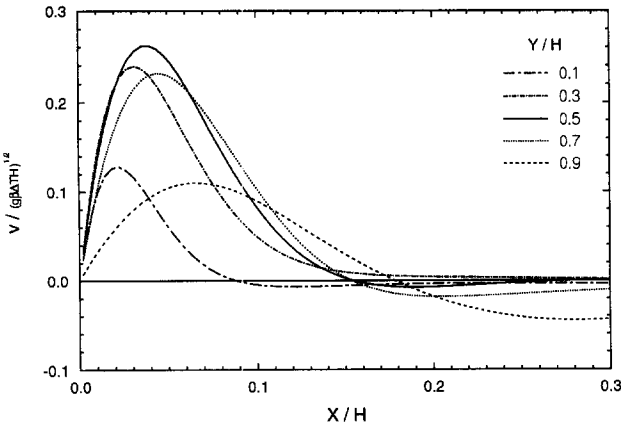

Figure 5 Vertical velocity profiles in the boundary layer along the hot wall as function of the distance x/H from the wall for various vertical positions y/H; the results are taken from the 240×240 simulation

The scaling of the quantities in Table 1 is suggested by Henkes, who showed that these scales are appropriate in the limit $\mathrm{Ra} \to \infty$.

At high spatial resolutions, the results of the lattice–Boltzmann simulations agree very well with the benchmark data of Le Quéré (1991). Le Quéré showed that his data are very accurate, because he found no change of the quantities in at least four significant digits from a grid refinement of 48×48 to 72×72 spectral functions. The computations by Janssen (1994) are performed using nonuniform grids that are strongly refined near the walls. At moderate resolutions (60^2 and 120^2), his results, therefore, agree better with those reported by Le Quéré (1991) than the results obtained with the lattice–Boltzmann scheme. In the core region of the flow, the stratification parameter S is slightly larger in the lattice–Boltzmann simulations compared to the results reported by Janssen (1994). This might be related to the much finer resolution in the core region of the present simulations because of the applied uniform grids.

The influence of the higher-order modes on the results of the lattice–Boltzmann simulations is investigated by varying the coefficients γ_2 and γ_3 within the range from 0.0 to 0.95 for a fixed resolution of 120×120 grid points. It has been found that the changes of the parameter values listed in Table 1 are limited to the fourth digit in $\mathrm{NuRa}^{-1/4}$, S and the vertical velocity component. The strongest influence is found in the horizontal velocity component, where changes occur up to the third digit. In our opinion, this relatively minor influence of the higher-order modes is due to the fact that the flow is laminar. In a turbulent flow where spatial variations and local gradients become much larger and where the fluid motion becomes (highly) irregular, the higher-order modes are presumably more important and proper minimization of these modes is required.

Finally, in Figures 5 and 6 the vertical velocity and temperature profiles in the boundary layer along the hot wall are shown as a function of x/H for various vertical positions y/H. The vertical velocity is scaled the same as in Table 1; whereas, the temperature is scaled with the temperature difference ΔT between the hot and cold wall. The boundary layer gradually develops and becomes thicker with increasing height. The x/H-location of extreme vertical velocity is shifted away from the wall with increasing y/H. The maximal vertical velocity is found around $y/H = 0.5$.

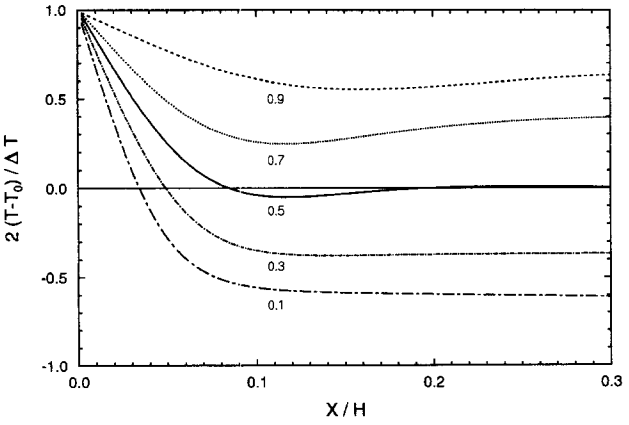

Figure 6 As in Figure 5, but for the temperature

Conclusions

The results of the simulations presented in this paper demonstrate that the lattice–Boltzmann scheme can be used successfully to study flows with scalar transport. The data for laminar free convective cavity flow reported here are in excellent agreement with numerical benchmark data reported earlier. The limitation to uniform grids seems to be a disadvantage of the lattice–Boltzmann scheme, but is in principle, inherent to it. This disadvantage is partly compensated for by the low computational effort per grid point. Recently, however, nonuniform extensions of the lattice–Boltzmann scheme have also become available, using a two-grid approach to alleviate the constraint of the original scheme to uniform and regular lattices. Nannelli and Succi (1992) and Succi and Nannelli (1994) showed that these extensions perform reasonably well in 2-D simulations, provided the underlying interpolation scheme is of sufficiently high order to avoid extensive numerical diffusion. The greater flexibility and more accurate representation of complex geometries, however, are gained at the expense of increased computational effort per grid point. Rigorous testing of the nonuniform lattice–Boltzmann scheme and actual application of it to 3-D problems will be unavoidable to guarantee future success of this extension.

On the other hand, we feel that the use of an uniform grid and the related high degree of isotropy of the scheme will prove to be favorable in large-eddy simulations where effects of scales smaller than the grid spacing must be modeled. Some preliminary results of large-eddy and direct numerical simulations of fully developed turbulent channel flow with heat transfer are available and compare favorably well with data available from simulations using different numerical techniques and with data available from experiments. The details and results of these simulations are beyond the scope of the present paper, but they indicate that the lattice–Boltzmann scheme is also suited for detailed, time-dependent, simulations of turbulent flows. In particular, the inherent capability to implement and run the scheme with great efficiency on massively parallel computer platforms turns out to be very promising for future large-scale simulations.

A final remark concerns the present implementation of the scalar transport equation in terms of scalar densities Q_i. This transport scheme is not very efficient with respect to computer memory usage. The ratio of physical modes available from Q_i, such as C, $\partial_x C$, and $\partial_y C$, and the number of entries stored in Q_i is much less (3/9 in 2-D and 4/18 in 3-D) than for the mass densities N_i (6/9 and 10/18 in 2-D and 3-D, respectively). In view of this, more efficient scalar transport schemes will be considered in the future as well.

References

Chen, S., Wang, J., Shan, X. and Doolen, G. 1992. Lattice–Boltzmann computational fluid dynamics in three dimensions. *J. Stat. Phys.*, **68**, 379

Eggels, J. G. M. 1994. Direct and large-eddy simulation of turbulent flow in a cylindrical pipe geometry. Ph.D. thesis, Delft University of Technology, The Netherlands

Frisch, U., d'Humières, D., Hasslacher, B., Lallemand, P., Pomeau, Y. and Rivet, J. P. 1987. Lattice–gas hydrodynamics in two and three dimensions. *Complex Systems*, **1**, 649–707

Henkes, R. A. W. M. 1990. Natural-convection boundary layers. Ph.D. thesis, Delft University of Technology, The Netherlands

d'Humières, D., Lallemand, P. and Frisch, U. 1986. Lattice gas models for 3-D hydrodynamics, *Europhys. Lett.*, **2**, 291–297

Janssen, R. J. A. 1994. Instabilities in natural-convection flows in cavities. Ph.D. thesis, Delft University of Technology, The Netherlands

Massaioli, F., Benzi, R. and Succi, S. 1993. Exponential tails in two-dimensional Rayleigh–Bénard convection. *Europhys. Lett.*, **21**, 305–310

McNamara, G. R. and Zanetti, G. 1989. Use of the Boltzmann equation to simulate lattice–gas automata. *Phys. Rev. Lett.*, **61**, 2332–2335

Nannelli, F. and Succi, S. 1992. The lattice–Boltzmann equation on irregular lattices. *J. Stat. Phys.*, **68**, 401

Le Quéré, P. 1991. Accurate solution to the square thermally driven cavity at high Rayleigh number. *Computers & Fluids* **20**, 29–41

Somers, J. A. 1993. Direct simulation of fluid flow with cellular automata and the lattice–Boltzmann equation. *Appl. Sci. Res.*, **51**, 127–133

Succi, S., Benzi, R., Vergassola, M. and Cancelliere, A. 1992. Hydrodynamic behavior of the lattice–Boltzmann equation. In *Numerical Methods for the Simulation of Multiphase and Complex Flow*, T. M. M. Verheggen (ed.), Lecture Notes in Physics, Vol. 398, Springer-Verlag, Berlin

Succi, S. and Nannelli, F. 1994. The finite volume formulation of the lattice–Boltzmann equation. *Trans. Theory and Stat. Phys.*, **23**, 163–171